

# Quantum Coherence Tomography of Lightwave–Controlled Superconductivity

L. Luo<sup>1\*</sup>, M. Mootz<sup>1,2\*</sup>, J. H. Kang<sup>3\*</sup>, C. Huang<sup>1</sup>, K. Eom<sup>3</sup>, J. W. Lee<sup>3</sup>, C. Vaswani<sup>1</sup>,  
Y. G. Collantes<sup>4</sup>, E. E. Hellstrom<sup>4</sup>, I. E. Perakis<sup>2</sup>, C. B. Eom<sup>3</sup> and J. Wang<sup>1†</sup>

<sup>1</sup>Department of Physics and Astronomy, Iowa State University,  
and Ames Laboratory, Ames, IA 50011 USA

<sup>2</sup>Department of Physics, University of Alabama at Birmingham,

<sup>3</sup>Department of Materials Science and Engineering, University of Wisconsin-Madison,  
Madison, WI 53706, USA

<sup>4</sup>Applied Superconductivity Center, National High Magnetic Field Laboratory,  
Florida State University, Tallahassee, FL 32310, USA.

\*Equal contribution

†To whom correspondence should be addressed; E-mail: jwang@ameslab.gov.

**Lightwave periodic driving of nearly dissipation-less currents has recently emerged as a universal control concept for both superconducting (SC) and topological electronics applications. While exciting progress has been made towards THz-driven superconductivity, our understanding of the interactions able to drive non-equilibrium pairing is still limited, partially due to the lack of direct measurements of high-order correlation functions. Such measurements would exceed conventional single-particle spectroscopies and perturbative responses to fully characterize quantum states far–from–equilibrium. Particularly, sensing of the exotic collective modes that would uniquely characterize lightwave-driven SC coherence, in a way analogous to the Meissner effect, is very challenging but much needed. Here we report the discovery**

**of lightwave-controlled superconductivity via *parametric* time-periodic driving of the strongly-coupled bands in iron-based superconductors (FeSCs) by a unique phase-amplitude collective mode assisted by broken-symmetry THz supercurrents. We are able to measure non-perturbative, high-order correlations in this strongly-driven superconductivity by separating the THz multi-dimensional coherent spectra (THz-MDCS) into conventional pump-probe, Higgs collective mode, and pronounced bi-Higgs frequency sideband peaks with highly nonlinear field dependence. We attribute the drastic transition in the coherent spectra to parametric excitation of time-dependent pseudo-spin canting states modulated by a phase-amplitude collective mode that manifests as a strongly nonlinear shift from  $\omega_{\text{Higgs}}$  to  $2\omega_{\text{Higgs}}$ . Remarkably, the latter higher-order sidebands dominate over the lower-order pump-probe and Higgs mode peaks above critical field, which indicates the breakdown of the susceptibility perturbative expansion in the parametrically-driven SC state. Correlation tomography by THz-MDCS provides opportunities for sensing of parametric quantum matter and non-equilibrium SC pairing that even processes finite center-of-mass momentum, with implications for THz supercurrent acceleration to extend gigahertz quantum circuits.**

Alternating “electromagnetic” bias, in contrast to DC bias, has shown promise to enable dynamical functionalities by terahertz (THz) modulation and control of topological-/super-currents and quantum order parameters during timescales faster than a cycle of lightwave oscillations [1–9]. THz-lightwave-accelerated SC and topological currents [8–17] have revealed exotic quantum dynamics, e. g., harmonic modes [9, 10, 18] and gapless quantum

fluid states [19] forbidden by equilibrium SC pairing symmetry, or light-induced Weyl and Dirac nodes [1, 14]. However, high-order correlation characteristics far exceeding the known two-photon light coupling to superconductors are hidden in conventional spectroscopy signals and perturbative responses, where a mixture of multiple excitation pathways contribute to the same low-order responses [20, 21]. A compelling solution to sensing SC coherence of light-driven states is to be able to identify unambiguously their collective modes [8, 22–27]. The dominant collective excitations of the equilibrium SC phase range from amplitude fluctuations (Higgs mode) to fluctuations of interband phase differences (Leggett mode) of the SC order parameter. Although amplitude modes have been observed close to equilibrium when external DC [17, 28, 29] and AC [9, 18] fields break inversion symmetry (IS), here we show that the phase coherent dynamics of the SC order parameters can parametrically drive quantum states, yet-to-be-observed, accessed by strong THz coherent two-pulse excitations. These states are characterized by distinct phase-amplitude collective modes arising from strong light-induced couplings between the amplitude and phase channels.

THz frequency, multi-dimensional coherent nonlinear spectroscopy (THz-MDCS) [11, 30–35] represents a correlation tomography tool to distinguish between different many-body response functions and light-induced collective modes in superconductors under strong two-pulse THz excitation. Unlike for THz-MDCS studies of semiconductors [11, 31, 32, 36], magnets [33], and molecular crystals [34], Fig. 1a illustrates three distinct features of our scheme in superconductors, not explored so far. *First*, our approach is based on measuring *the phase of the supercurrent coherent nonlinear emission*, in addition to the amplitude, by using phase-resolved coherent measurements with two *intense* phase-locked THz pulses of *similar* field strengths that has not been applied on superconductors. Taking advantage of both the real time and the relative phase of the two THz fields, we separate in two-dimensional (2D) frequency space spectral peaks generated by light-induced correlations and collective mode interactions

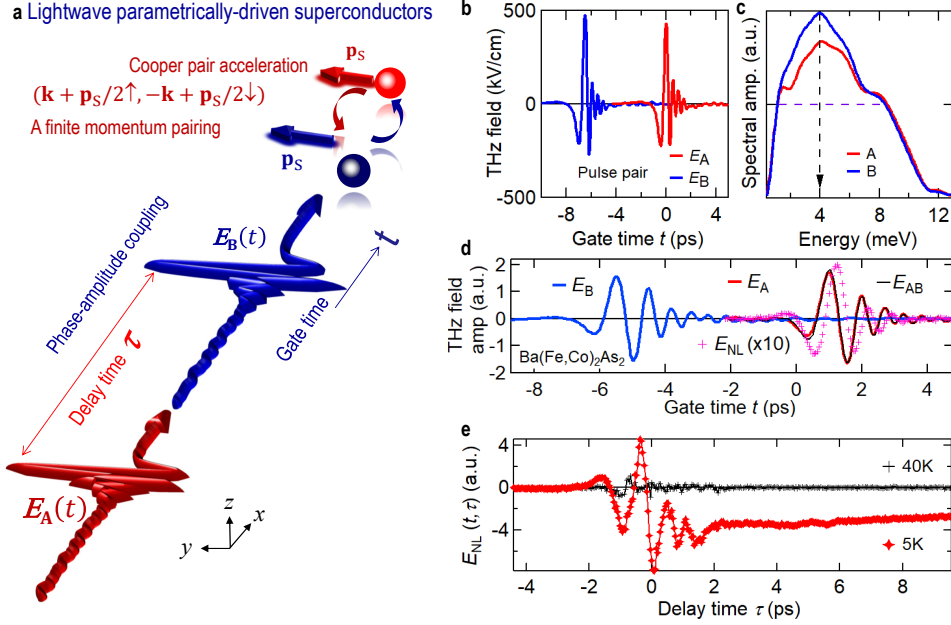


**Fig. 1. Terahertz (THz) multidimensional coherent spectroscopy of lightwave accelerated non-equilibrium superfluid states in FeSCs.** a, Schematics of lightwave supercurrent generation, coherent control and detection of the parametrically-driven SC state via two phase-locked THz pulses in our experiment. b, Temporal waveforms of the nearly single-cycle THz pulse-pair used in the experiment (red and blue lines), and c, spectra of the used pulses, centered at  $\omega_0 = 4$  meV. d, Temporal dynamics of the measured coherent nonlinear transmission  $E_{NL}(t, \tau)$  (pink) =  $E_{AB}(t, \tau)$  (black) -  $E_A(t)$  (red) -  $E_B(t, \tau)$  (blue) as a function of gate time  $t$  at a fixed delay time between the two pulses,  $\tau = 6.5$  ps, under THz driving fields of 229 kV/cm at temperature of 5 K. e, Temporal dynamics of the  $E_{NL}(t, \tau)$  amplitude decay below (red diamond, 5 K) and above (black cross, 40 K)  $T_c$ , as a function of pulse-pair time delay  $\tau$  under THz driving fields of 333 kV/cm. The correlated nonlinear signal  $E_{NL}(t, \tau)$  (red) decays over timescales much longer than the pulse duration.

from the conventional pump–probe, four–wave–mixing, and high–harmonic–generation signals [9, 23]. This 2D separation of spectral peaks arising from high–order nonlinear processes achieves a “super” resolution of many-body interactions and collective modes in highly non-perturbative states, which is not possible with the conventional spectroscopy one-dimensional measurements of prior works [9, 19, 23]. *Second*, as a result of lightwave condensate acceleration by the effective local field inside a thin–film SC induced by two sub-gap THz pulses and electromagnetic propagation effects, the Cooper pairs ( $\mathbf{k}$ ,  $-\mathbf{k}$ ) of the equilibrium BCS state experience a highly nonlinear center–of–mass momentum,  $\mathbf{p}_S(t)$ , i. e., SC pairing with finite center-of-mass momentum (Fig. 1a). Precisely, the state persists well after the two strong pulses and results in  $(\mathbf{k} + \mathbf{p}_S(t)/2, -\mathbf{k} + \mathbf{p}_S(t)/2)$  Cooper pairing, due to dynamical symmetry breaking of the centrosymmetric pairing states [9]. *Third*, the driven quantum state with current-flow  $\propto \mathbf{p}_S(t)$  controllable by two–pulse interference can host distinct collective modes that provide parametric excitation of the time-dependent quantum states (Fig. 1a), whose nonlinear interactions determine the THz–MDCS spectral profile [37].

In this Article, we reveal a superconducting state parametrically driven by time–periodic light–induced dynamics of the order parameter phase in a  $\text{Ba}(\text{Fe}_{1-x}\text{Co}_x)_2\text{As}_2$  superconductor. Such parametric driving becomes important when the phase dynamics is amplified by a phase–amplitude collective mode that develops with increasing THz pulse–pair driving. The change in the character of the SC state manifests itself via the drastic changes in the THz–MDCS spectra observed with increased two–pulse driving. In particular, we observe a transition in THz–MDCS, from wave–mixing peaks centered at the Higgs amplitude mode frequency  $\omega_H$  to bi–Higgs frequency sidebands at  $2\omega_H$ . Remarkably, the higher–order  $2\omega_H$  peaks dominate over the lower order single–Higgs peaks and conventional pump–probe spectra above critical THz field strength. We attribute the non–perturbative sidebands at bi–Higgs frequencies to the parametrically driven SC state by the collective temporal oscillations in the phases of the

$s_{\pm}$ -symmetry order parameter, consistent with our quantum kinetic simulations.

We measured optimally Co-doped BaFe<sub>2</sub>As<sub>2</sub> (Ba-122) epitaxial thin film (60 nm) with  $T_c \sim 23$  K and lower SC gap  $2\Delta_1 \sim 6.8$  meV (Methods section 1.1). We used THz-MDCS to measure the responses to two phase-locked, nearly single-cycle THz pulses A and B of similar field strength (Fig. 1b), with central frequency  $\omega_0 \sim 4$  meV (black arrow, Figs. 1c) and broadband frequency width of  $\Delta\omega \sim 6$  meV (purple dashed line, Fig. 1c) (Methods section 1.2). Representative time scans of these THz-MDCS experiments driven by laser fields  $E_{\text{THz,A,B}} = 229$  kV/cm, are shown in Fig. 1d. The measured nonlinear differential emission correlated signal,  $E_{\text{NL}}(t, \tau) = E_{\text{AB}}(t, \tau) - E_{\text{A}}(t) - E_{\text{B}}(t, \tau)$ , was recorded as a function of both the gate time  $t$  (Fig. 1d) and the delay time  $\tau$  between the two pulses A and B (Fig. 1e). We note three points. First, as demonstrated by  $E_{\text{NL}}(t, \tau)$  shown in Fig. 1d (pink cross), measured at fixed delay  $\tau = 6.5$  ps, the electric field in the time domain allows for simultaneous amplitude-/phase-resolved detection of the coherent nonlinear responses induced by the pulse-pair and has negligible contributions from the individual pulses. This is achieved by subtracting the individual responses,  $E_{\text{A}}(t)$  and  $E_{\text{B}}(t, \tau)$  (red and blue solid lines), from the full signal obtained in response to both phase-locked pulses,  $E_{\text{AB}}(t, \tau)$  (black solid line). Second, the  $E_{\text{NL}}(t, \tau)$  in Fig. 1e vanishes above the SC transition temperature  $T_c$ , as seen by comparing the 5 K (red diamond) and 40 K traces (black cross). Third, the THz-MDCS signals persist even when the two pulses do not overlap in time, e. g., at  $\tau = 6.5$  ps (Figs. 1d–1e). The long-lived correlated signal  $E_{\text{NL}}(t, \tau)$  indicates that the two sub-gap laser excitations, centered below  $2\Delta_1$  (Fig. 1c), have generated robust supercurrent-carrying macroscopic states persisting well after the pulse.

Figure 2 compares the 2D THz temporal profile of the coherent nonlinear signal  $E_{\text{NL}}(t, \tau)$  for relatively weak (Fig. 2a), intermediate (Fig. 2b), and strong (Fig. 2c) driving fields. The  $E_{\text{NL}}(t, \tau)$  dynamics reveals that pronounced coherent temporal oscillations last much longer than the temporal overlap between the two driving pulses (Fig. 1b). These long-lived coherent

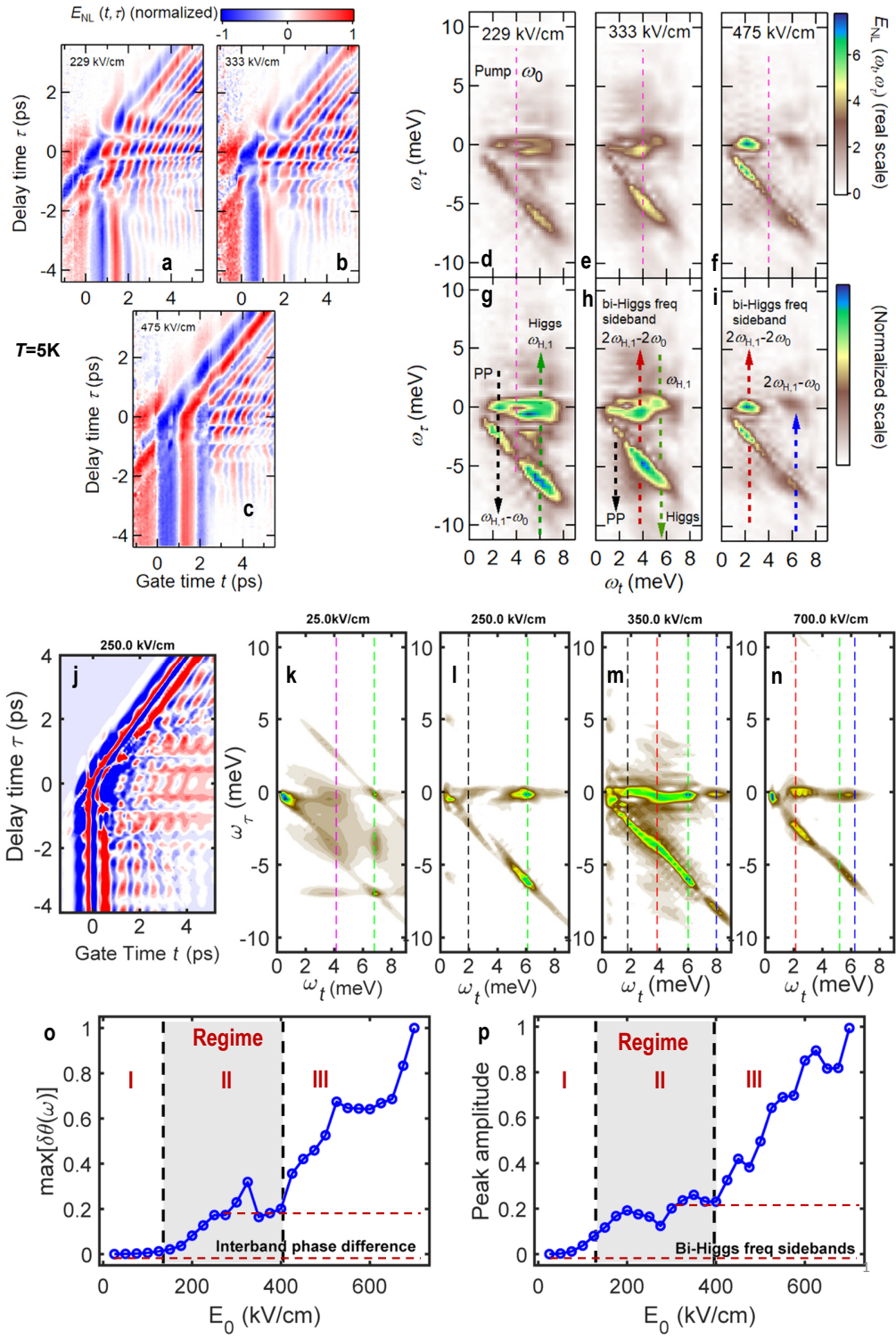


**Fig. 2. Drastic changes of correlations and collective modes revealed in the driving electric field dependence of THz-MDCS.** a-c, Two-dimensional (2D) false-colour plot of the measured coherent nonlinear transmission  $E_{\text{NL}}(t, \tau)$  of FeSCs superconductors at 5 K induced by THz pump electric fields of (a) 229 kV/cm, (b) 333 kV/cm and (c) 475 kV/cm. d-f, The corresponding THz 2D coherent spectra  $E_{\text{NL}}(\omega_t, \omega_\tau)$  at 5 K for the above three pump electric fields, respectively. g-i, The normalized  $E_{\text{NL}}(\omega_t, \omega_\tau)$  spectra are plotted for the same pump fields to highlight the pump field-dependent evolution of the correlation peaks along the 2D frequency vector space. Peaks marked by the dashed lines are located at frequencies associated with the Higgs (green) mode and bi-Higgs frequency sideband (red and blue) consistent with the theory. j, An example of calculated  $E_{\text{NL}}(t, \tau)$  as a function of gate time  $t$  and delay time  $\tau$  for 250 kV/cm pump field. k-n, 2D Fourier transform of  $E_{\text{NL}}(t, \tau)$ . As predicted by the theory, dashed black (blue) lines indicate pump-probe  $\omega_t = \omega_{\text{H},1} - \omega_0$  (bi-Higgs frequency sideband  $\omega_t = 2\omega_{\text{H},1} - \omega_0$ ) while IS-breaking signals at Higgs  $\omega_t = \omega_{\text{H},1}$  (bi-Higgs frequency sideband  $\omega_t = 2\omega_{\text{H},1} - 2\omega_0$ ) are marked by vertical dashed green (red) line; pump-probe peaks at  $\omega_t = \omega_0$  are indicated by vertical dashed magenta lines. o, Field-strength dependence of the dominant peak in the spectrum of the interband phase difference  $\delta\theta(\omega)$ . p, Field-strength dependence of the bi-Higgs frequency sidebands at  $2\omega_{\text{H},1} - \omega_0$  follows the  $\delta\theta(\omega)$  behavior in (o), which identifies the importance of light-induced time-periodic phase dynamics at the  $\omega_{\text{H},1}$  frequency in driving a non-equilibrium SC state. Three excitation regimes are marked (main text).

responses generate sharp THz-MDCS spectral peaks visible up to  $\sim 8$  meV below substrate absorption (Methods). These spectra were obtained by Fourier transform of  $E_{\text{NL}}(t, \tau)$  with respect to both  $t$  (frequency  $\omega_t$ ) and  $\tau$  (frequency  $\omega_\tau$ ) (Figs. 2d–2f). We observe multiple distinguishing and well-defined resonances with unique lineshapes that drastically change with increasing field strength. These  $E_{\text{NL}}(\omega_t, \omega_\tau)$  spectra differ strongly from the conventional ones measured, e. g., in semiconductors [11, 31, 32]. In the latter uncorrelated systems, peaks are observable at multiples of the THz driving pulse frequency  $\omega_0 \sim 4$  meV (magenta dashed line), as expected in the case of a rigid excitation energy bandgap. The observed peaks in FeSCs are much narrower than the excitation pulse width  $\Delta\omega$  (Fig. 1c). This result implies that  $E_{\text{NL}}(t, \tau)$  oscillates with the frequencies of SC collective mode excitations that lie within the  $\Delta\omega$  of the few-cycle driving pulses, with the width of the THz-MDCS spectral peaks determined by the SC mode damping and not by  $\Delta\omega$  of the driving pulses.

The normalized  $E_{\text{NL}}(\omega_t, \omega_\tau)$  experimental spectra shown in Figs. 2g–2i visualize nonlin-



ear couplings of SC collective mode resonances and their field-dependences. For the weaker pump field of  $E_0 = 229$  kV/cm in Fig. 2g, the THz-MDCS spectrum shows four dominant peaks. Intriguingly, the two strongest peaks are located at the higher frequencies, roughly  $(6, 0)$  meV and  $(6, -6)$  meV, with the weaker peaks at the lower frequencies, slightly below  $(2, 0)$  meV and  $(2, -2)$  meV. This observation is in strong contrast to the expectation from conventional harmonic generation that high-order nonlinear signals should be weaker than lower-order ones. Such a reversal of coherent nonlinear signal strengths indicates a breakdown of a susceptibility perturbative expansion around the SC equilibrium state. For the intermediate field of  $E_0 = 333$  kV/cm (Fig. 2h), the THz-MDCS spectrum shows several peaks close to each other (red and green lines), centered at new frequencies  $\sim (5, 0)$  meV and  $(5, -5)$  meV which exhibit the similar non-perturbative behavior with dominant high order THz-MDCS spectral peaks. The spectral profile changes again with increasing THz driving: four peaks are observable in the THz-MDCS spectrum for the highest studied pump field of  $E_0 = 475$  kV/cm. For such high fields, the two strongest THz-MDCS peaks are roughly located at  $(2.3, 0)$  meV and  $(2.3, -2.3)$  meV, while two weaker peaks become detectable at higher frequencies, at  $(6.2, 0)$  meV and  $(6.2, -6.2)$  meV (Fig. 2i). These high field peaks should be distinguished from the low field ones at similar frequencies (Fig. 2g), as the latter have red-shifted with increasing field due to the SC gap reduction. The evolution of the well-defined MDCS spectral peaks reflect the emergence of different collective modes with increasing driving field, which characterize the transition to different non-equilibrium SC states.

We use three principles to classify the observed peaks in  $(\omega_t, \omega_\tau)$  space. First, we introduce frequency vectors characterizing the two pulses A and B,  $\omega_A = (\omega_0 \pm \Delta\omega, 0)$  and  $\omega_B = (\omega_0 \pm \Delta\omega, -\omega_0 \mp \Delta\omega)$ , which are centered around  $\omega_0 \sim 4$  meV (black arrow, Fig. 1c). The corresponding “time vectors”  $t' = (t, \tau)$  allow us to represent the driving electric fields of Fig. 1b in the form  $\mathbf{E}_A(t') \sin(\omega_A t')$  and  $\mathbf{E}_B(t') \sin(\omega_B t')$ , respectively. Second, the non-equilibrium

SC state driven by the above pulse-pair is characterized by a quenched asymptotic value of the time-evolved SC order parameter, which defines the Higgs frequencies  $\omega_{H,i} = 2\Delta_{\infty,i}$ , where  $i = 1$  ( $i = 2$ ) denotes the hole (electron) pocket of the FeAs bandstructure. The above Higgs mode frequencies decrease from their equilibrium values of  $2\Delta_{0,i}$  with increasing field, which leads to a redshift of the THz-MDCS spectral features observed in Figs. 2g–2i. Note that we only probe the lower Higgs mode,  $\omega_{H,1} \sim 6.8$  meV, while the higher Higgs frequency,  $\omega_{H,2} \sim 19$  meV, lies outside of the measured spectral range (Fig. 1c). Third, the THz pulses drive the Anderson pseudospin oscillators [9, 35] at the different momenta  $\mathbf{k}$  (Methods section 1.4), whose dynamics is dominated by frequencies  $\sim \omega_{H,i;A} = (\omega_{H,i}, 0)$  and  $\sim \omega_{H,i;B} = (\omega_{H,i}, -\omega_{H,i})$ , i. e., field-dependent Higgs and quasi-particle pair excitations, or  $\sim 2\omega_{A,B}$ , i. e., quasi-particle excitations driven at the laser frequency.

To identify which nonlinear process generates each peak measured in Figs. 2g–2i, we use our quantum kinetic simulations (Methods section 1.3) and the above three principles. Light-wave propagation inside a SC thin film geometry determines the effective driving field  $E(t) = E_{\text{THz}}(t) - \frac{\mu_0 c}{2n} J(t)$ , which is obtained from Maxwell's equations [37] and differs from the applied field  $E_{\text{THz}}(t)$  ( $n$  is the refractive index). This effective field drives the nonlinear supercurrent  $J(t)$ , described self-consistently by solving the gauge-invariant SC Bloch equations [23, 35, 37] (Methods section 1.3) for a 3-pocket SC model with strong electron-hole pocket interaction  $U$  far exceeding the intra-band pairing interaction. Using the above results, we simulate directly the  $E_{\text{NL}}(t, \tau)$  temporal dynamics measured in the experiment (Fig. 2j as an example) and then obtain the  $E_{\text{NL}}(\omega_t, \omega_\tau)$  spectra (Figs. 2k–2n). These simulations are fully consistent with the observed drastic change in the THz-MDCS spectra, where non-perturbative spectral peaks emerging with increasing field, as shown in Figs. 2g–2i, are indicative of a transition to light-driven SC states with different, emergent collective modes.

We elaborate the above quantum state transition by using three different excitation regimes,

marked in Figs. 2o (red arrows) as field-strength dependence of the interband phase difference  $\delta\theta(\omega)$  peak: I, perturbative regime; II, the non-perturbative state with dominant Higgs amplitude mode; regime III, the parametrically-driven SC state determined by phase–amplitude collective mode. We first examine the perturbative susceptibility regime I, where the Higgs frequency  $\omega_{H,1}$  remains close to its equilibrium value,  $2\Delta_1 \sim 6.8$  meV, similar to the “rigid” excitation energy gap in semiconductors. The simulated THz-MDCS spectrum (Fig. 2k) then shows several peaks (Table 1, Methods) splitting along the  $\omega_\tau$  vertical axis, at  $\omega_t = \omega_0$  (dashed magenta line) and  $\omega_t = \omega_{H,1}$  (dashed green line). The conventional pump–probe signals are observed at  $(\omega_0, -\omega_0)$  and  $(\omega_0, 0)$  in Fig. 2k, generated by the familiar third-order processes  $\omega_A - \omega_A + \omega_B$  and  $\omega_B - \omega_B + \omega_A$ , respectively. Four-wave mixing signals are also observed at  $(\omega_0, \omega_0)$  and  $(\omega_0, -2\omega_0)$ , generated by the third-order processes  $2\omega_A - \omega_B$  and  $2\omega_B - \omega_A$ . However, the perturbative behavior in this regime are inconsistent with the dominance of higher-order peaks (Fig. 2g) for the much stronger fields used in the experiment to achieve the necessary signal-to-noise ratio.

By increasing the field strength (Figs. 2l–2n), the calculated signals along the  $\omega_\tau$  vertical axis and at  $(\omega_0, -\omega_0)$ ,  $(\omega_0, 0)$  diminish. Only peaks along  $(\omega_t, 0)$  and  $(\omega_t, -\omega_t)$  are then predicted by our calculation, consistent with the experiment in Figs. 2g–2i. For the lower field strength of 250 kV/cm (Fig. 2l), our calculated THz-MDCS spectrum shows two weak peaks at  $\omega_t \sim 2$  meV (black dashed line) and two strong broken-IS peaks at  $\omega_t = \omega_{H,1} \sim 6$  meV (green dashed line), similar to the experimental THz-MDCS peaks shown in Fig. 2g. The weak peaks at  $\omega_t \sim 2$  meV (black dashed line) arise from high-order difference-frequency Raman processes (PP, Table 2 in Methods), which generate pump–probe signals at  $\omega_t = \omega_{H,1} - \omega_0$ , as observed in Figs. 2d and 2g. The strong peaks at the Higgs frequency  $\omega_t = \omega_{H,1} \sim 6$  meV (green dashed line) dominate for intermediate fields up to  $\sim 400$  kV/cm (regime II, Fig. 2o), but vanish if we neglect the electromagnetic propagation effects as discussed later. The BCS ground state evolves into a finite-momentum-pairing SC state, which is determined by the condensate

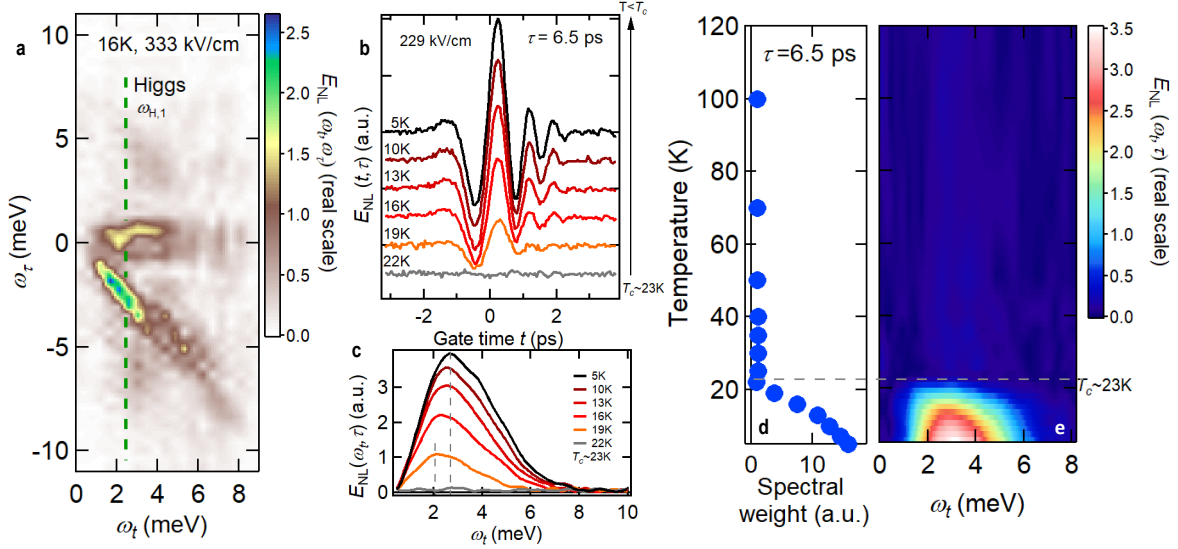


**Fig. 3. Temperature dependence of THz-MDCS signals.** a, THz-MDCS spectra  $E_{\text{NL}}(\omega_t, \omega_\tau)$  at 16 K for pump electric field 333 kV/cm. b, Temporal profiles of two-pulse THz coherent signals  $E_{\text{NL}}(t, \tau)$  at various temperatures from 5 K to 22 K for a peak THz pump electric field of  $E_{\text{pump}} = 229$  kV/cm and  $\tau = 6.5$  ps. Traces are offset for clarity. c, The corresponding Fourier spectra of the coherent dynamics in (b). d-e, A 2D false-color plot of THz coherent signals (e) as a function of temperature and frequency  $\omega_t$  with (d) integrated spectral weight at various temperatures. Dashed gray line indicates the SC transition temperature.

momentum  $\mathbf{p}_S$  generated by third-order nonlinear processes (Supplementary Fig. 4c, Note 4) and persisting well after the pulse. Higgs frequency peaks then arise from ninth-order IS breaking nonlinear processes generated by the coupling between the Higgs mode and the lightwave accelerated supercurrent  $J(t)$  (IS Higgs, Table 2 in Methods). The superior resolution achieved for sensing the collective modes using THz-MDCS with 2D coherent excitation is far more than a static IS symmetry breaking scheme using a DC current (Supplementary Fig. 9, Note 7).

For an even higher field strength of 350 kV/cm (Fig. 2m) and of 700 kV/cm (Fig. 2n), the THz-MDCS spectra change above the excitation threshold where the order parameter phase

dynamics becomes significant, as shown in Fig. 2o (regime III). As discussed in Methods (section 1.4), time-periodic phase deviations from their equilibrium values, with frequency  $\omega_{H,1}$ , parametrically drive pseudo-spin time-dependent canting (Supplementary Fig. 4d), which coincides with a highly nonlinear field-dependence of  $\mathbf{p}_S$  (Supplementary Fig. 4c). In this regime III, new dominant THz-MDCS peaks emerge at  $\omega_t = 2\omega_{H,1} - \omega_0$  (blue dashed line), referred as to bi-Higgs frequency sideband, while satellite peaks are also observed at  $\omega_t = 2\omega_{H,1} - 2\omega_0$  (red dashed line). The spectral position of these emergent sideband peaks in 2D frequency space indicates that they arise from a second harmonic of the Higgs frequency,  $2\omega_{H,1}$ . Figure 2p demonstrates a threshold nonlinear behavior of these bi-Higgs frequency sideband peak strengths, which coincides with the development of strong phase dynamics as seen in Fig. 2o.

These theoretical prediction are fully consistent with our experimental observations in Figs. 2h and 2i. For the intermediate field in Fig. 2m, the THz-MDCS peaks at  $\omega_t = 2\omega_{H,1} - 2\omega_0 \sim 4$  meV (red dashed line) and  $\omega_t = \omega_{H,1} \sim 6$  meV (green dashed line) are close to each other, so they merge into a single broad resonance around  $(5, 0)$  meV and  $(5, -5)$  meV in the calculated 2D spectrum. This result agrees with the measured broad, overlapping THz-MDCS peaks  $\sim 5$  meV in Fig. 2h, while the calculated  $\omega_t = 2\omega_{H,1} - \omega_0$  peak (blue line) is not visible experimentally due to the substrate absorption. For the highest studied field strength (Fig. 2n), the calculated THz-MDCS signals are dominated by the bi-Higgs frequency nonlinear sidebands at  $\omega_t = 2\omega_{H,1} - \omega_0 \sim 6.0$  meV and  $\omega_t = 2\omega_{H,1} - 2\omega_0 \sim 2.0$  meV. Both sidebands peaks now fall into the substrate transparency region and are clearly resolved in Fig. 2i. The emergence of these new MDCS peaks in Regime III will be discussed later as manifestations of a phase-amplitude collective mode that parametrically drive pseudo-spin canting with respect to the  $s_{\pm}$ -symmetry equilibrium directions.

Figure 3 demonstrates the strong temperature dependence and redshift of the observed peaks as we approach  $T_c$ . The THz-MDCS spectrum  $E_{NL}(\omega_t, \omega_{\tau})$  at temperature 16 K is shown in

Fig. 3a for the intermediate field of  $E_0 = 333$  kV/cm, and is compared in Fig. 2h with the spectrum at  $T=5$  K for same excitation. The broken-IS signals observed at the Higgs mode frequency  $\omega_t = \omega_{H,1}$  red-shift with increasing temperature, from  $(5, 0)$  meV and  $(5, -5)$  meV peaks at 5 K to broad peaks slightly below  $(2.5, -2.5)$  meV and  $(2.5, 0)$  meV at 16 K (green line). This redshift arises from the thermal quench of the SC order parameter  $2\Delta_1$  with increasing temperature. However, unlike for the case of THz coherent control of the order parameter demonstrated in Fig. 2h, a thermal quench does not produce any obvious bi-Higgs frequency THz-MDCS peaks expected  $\sim 1$  meV, which is indicative of the coherent origin of the latter. Figures 3b and 3c show the temperature dependence of the measured differential coherent emission  $E_{\text{NL}}(t, \tau)$  and the corresponding  $E_{\text{NL}}(\omega_t, \tau)$  at a fixed pulse separation  $\tau = 6.5$  ps. It is clearly seen, by comparing the 5 K (black line) and 22 K (gray) traces, that, when approaching  $T_c$  from below, the coherent nonlinear emissions quickly diminish and red-shift. Finally, Figs. 3d–3e show a detailed plot of  $E_{\text{NL}}(\omega_t, \tau)$  up to 100 K. The integrated spectral weight shown in Fig. 3d correlates with the SC transition at  $T_c$  (gray dashed line).

Figure 4 offers more insight into the physical mechanism behind the observed transition in the THz-MDCS spectra with increasing field. First, we compare the spectra  $E_{\text{NL}}(\omega_t, \omega_\tau)$  for a field strength of 250 kV/cm between (i) the full calculation that includes electromagnetic propagation and interference effects leading to slowly decaying  $p_S(t)$  after the pulse (Fig. 4a), and (ii) a calculation where these effects are switched off, in which case  $p_S(t)$  oscillates during the THz pulse and vanishes afterwards (Fig. 4b). In the latter case, the  $\omega_t = \omega_{H,1}$  peak vanishes in Fig. 4b (green dashed line), and the THz-MDCS spectrum is dominated by broad pump-probe (PP) peaks at  $\omega_t = \omega_0 \sim 4$  meV, similar to Fig. 2k. This result suggests that the peaks at  $\omega_{H,1}$  dominating the PP peaks in nonlinear regime II, as in Fig. 2g (data) and Fig. 4a (theory), provide coherent sensing of non-perturbative Higgs collective modes underpinning the finite-momentum-pairing SC phase (Supplementary Note 7) different from the ground state in

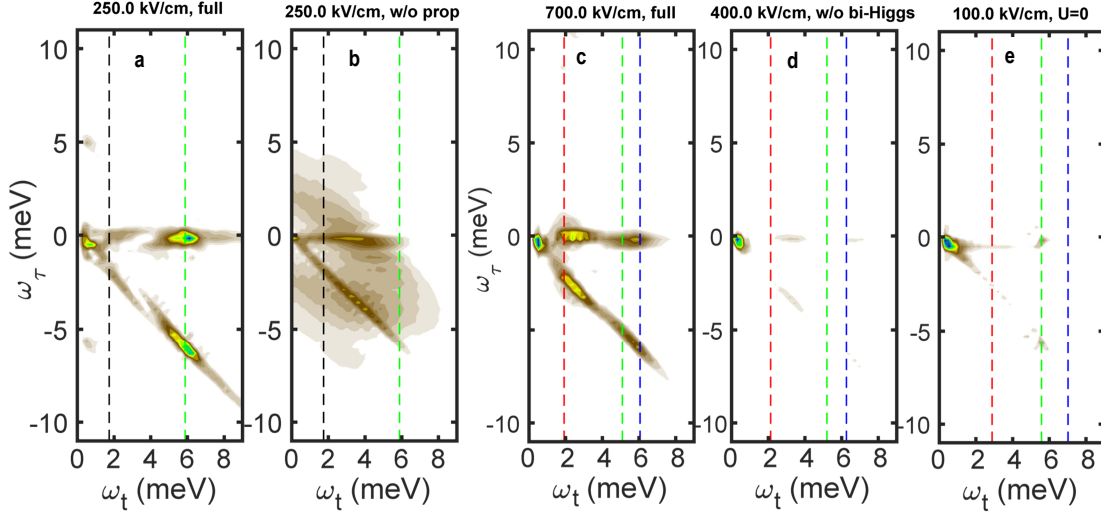


**Fig. 4. Origin of correlation and collective mode peaks in THz-MDCS signals underpinned by switch-off analysis.** a-b,  $E_{\text{NL}}(\omega_t, \omega_\tau)$  for (a) the full calculation with lightwave propagation ( $E_0 = 250$  kV/cm) and for (b) a calculation without propagation ( $E_0 = 250$  kV/cm). Dashed black (green) lines indicate  $\omega_t = \omega_{\text{H},1} - \omega_0$  ( $\omega_t = \omega_{\text{H},1}$ ). The IS peaks at  $\omega_t = \omega_{\text{H},1}$  vanish without persisting IS breaking. c-e,  $E_{\text{NL}}(\omega_t, \omega_\tau)$  for (c) the full calculation with lightwave propagation ( $E_0 = 700$  kV/cm), for (d) a calculation without phase–amplitude coupling ( $E_0 = 400$  kV/cm), and for (e) a calculation without interband interaction,  $U = 0$  ( $E_0 = 100$  kV/cm). To directly compare the different THz-MDCS spectra, the field strengths of the different calculations are chosen such that  $\omega_{\text{H},1}$  are comparable,  $\omega_{\text{H},1} \sim 5.0$  meV. Dashed blue lines indicate  $\omega_t = 2\omega_{\text{H},1} - \omega_0$ , while IS-breaking signals at Higgs  $\omega_t = \omega_{\text{H},1}$  (bi-Higgs  $\omega_t = 2\omega_{\text{H},1} - 2\omega_0$ ) are marked by vertical dashed green (red) lines. Note that the bi-Higgs frequency sideband peaks are strongly suppressed without phase–amplitude coupling or without interband interaction.

perturbative regime I. Next, we turn to the transition from Higgs to dominant bi-Higgs signals at  $\omega_t = 2\omega_{H,1} - \omega_0$ . We associate this transition with the development of a time-dependent canted pseudo-spin state, which is parametrically-driven by amplified phase dynamics at frequency  $\omega_{H,1}$ . The nonlinear enhancement of this phase dynamics in regime III originates from the development of a phase-amplitude collective mode at  $\omega_{H,1}$  (Figs. 2o and 2p). This phase-amplitude mode interacts with a quasi-particle excitation, both with energies  $\sim \omega_{H,1}$ , which amplifies the THz-MDCS sideband peaks at frequencies  $\sim 2\omega_{H,1}$  (Fig. 2n), at the expense of the Higgs mode peak at  $\omega_{H,1}$  which dominates in regime II.

We attribute the drastic change in the THz-MDCS spectra with the non-perturbative emergence of the bi-Higgs frequency sideband in Regime III over the Higgs peak to parametric excitation of time-dependent pseudo-spin canting modulation by a phase-amplitude collective mode (Methods sections 1.4 and 1.5). The latter collective mode develops above critical excitation and leads to pronounced phase dynamics at the Higgs frequency  $\omega_{H,1}$  (Supplementary Figs. 4a and 4b). To further corroborate the transition from Higgs amplitude to phase-amplitude collective mode, we compare in Figs. 4c and 4d the spectra  $E_{NL}(\omega_t, \omega_\tau)$  obtained from the full calculation for 700.0 kV/cm driving with those obtained by turning off the pseudo-spin canting driven by the  $\omega_{H,1}$  time-periodic phase fluctuations around the  $s_\pm$  equilibrium state (Supplementary Figs. 4d and 6, Note 4). Our formulation of the gauge-invariant SC Bloch equations in terms of two coupled pseudo-spin nonlinear oscillators, presented in the Methods section 1.4, shows that non-adiabatic pseudo-spin canting is parametrically driven with time-dependent strength  $\sim |\Delta_1|^2 \sin(2\delta\theta)$ . The threshold nonlinear field dependence of this coupling, shown in Supplementary Fig. 4d, leads to the strong field dependence of the  $\sim 2\omega_{H,1}$  sideband (Fig. 2p). By comparing Figs. 4c and 4d, we see that the signals at frequencies  $\omega_t = 2\omega_{H,1} - \omega_0$  (blue dashed line) and  $\omega_t = 2\omega_{H,1} - 2\omega_0$  (red dashed line) are absent when the order parameter phase can be approximated by its equilibrium value. We also compare the full result with a calculation



without interband Coulomb interaction between the electron and hole pockets (Fig. 4e), which diminishes the bi-Higgs frequency signals. If the inter-band Coulomb coupling exceeds the intra-band pairing interaction, the Leggett mode phase oscillations lie well within the quasi-particle continuum (regime I), so they are overdamped (Fig. 2o). Above critical THz driving (regime III), however, the THz-modulated superfluid density of strongly-Coulomb-coupled electron and hole pockets (Methods section 1.5 and Supplementary Note 4) enhances the non-linear coupling between the phase-amplitude collective mode ( $\omega_{H,1}$ ) and quasi-particle excitations ( $\omega_{H,1}$ ) in the parametrically-driven SC state that processes supercurrent  $J(t)$ -oscillations at  $2\omega_{H,1}$  visualized as the unique bi-Higgs sidebands in the THz-MDCS spectra (Fig. 2i).

## References

- [1] Vaswani, C. *et al.* Light-driven Raman coherence as a nonthermal route to ultrafast topology switching in a Dirac semimetal. *Phys. Rev. X* **10**, 021013 (2020).
- [2] Fausti, D. *et al.* Light-induced superconductivity in a stripe-ordered cuprate. *Science* **331**, 189–191 (2011).
- [3] Knap, M., Babadi, M., Refael, G., Martin, I. & Demler, E. Dynamical Cooper pairing in nonequilibrium electron-phonon systems. *Phys. Rev. B* **94**, 214504 (2016).
- [4] Mitrano, M. *et al.* Possible light-induced superconductivity in  $K_3C_6O$  at high temperature. *Nature* **530**, 461–464 (2016).
- [5] Budden, M. *et al.* Evidence for metastable photo-induced superconductivity in  $_3C_6O$ . *Nature Physics* **17**, 611–618 (2021).
- [6] Isoyama, K. *et al.* Light-induced enhancement of superconductivity in iron-based superconductor  $FeSe_{0.5}Te_{0.5}$ . *Communications Physics* **4**, 160 (2021).

- [7] Buzzi, M. *et al.* Higgs-mediated optical amplification in a nonequilibrium superconductor. *Phys. Rev. X* **11**, 011055 (2021).
- [8] Matsunaga, R. *et al.* Light-induced collective pseudospin precession resonating with Higgs mode in a superconductor. *Science* **345**, 1145–1149 (2014).
- [9] Yang, X. *et al.* Lightwave-driven gapless superconductivity and forbidden quantum beats by terahertz symmetry breaking. *Nat. Photon.* **13**, 707–713 (2019).
- [10] Linder, J. & Robinson, J. W. Superconducting spintronics. *Nat. Phys.* **11**, 307 (2015).
- [11] Maag, T. *et al.* Coherent cyclotron motion beyond Kohn’s theorem. *Nature Physics* **12**, 119–123 (2016).
- [12] Reimann, J. *et al.* Subcycle observation of lightwave-driven Dirac currents in a topological surface band. *Nature* **562**, 396–400 (2018).
- [13] Lingos, P. C., Kapetanakis, M. D., Wang, J. & Perakis, I. E. Light-wave control of correlated materials using quantum magnetism during time-periodic modulation of coherent transport. *Communications Physics* **4**, 60 (2021).
- [14] Luo, L. *et al.* A light-induced phononic symmetry switch and giant dissipationless topological photocurrent in ZrTe<sub>5</sub>. *Nat. Mater.* **20**, 329–334 (2021).
- [15] Rajasekaran, S. *et al.* Parametric amplification of a superconducting plasma wave. *Nat. Phys.* **12**, 1012–1016 (2016).
- [16] Dienst, A. *et al.* Bi-directional ultrafast electric-field gating of interlayer charge transport in a cuprate superconductor. *Nature Photon.* **5**, 485–488 (2011).

- [17] Nakamura, S. *et al.* Infrared activation of the Higgs mode by supercurrent injection in superconducting NbN. *Phys. Rev. Lett.* **122**, 257001 (2019).
- [18] Vaswani, C. *et al.* Terahertz second-harmonic generation from lightwave acceleration of symmetry-breaking nonlinear supercurrents. *Phys. Rev. Lett.* **124**, 207003 (2020).
- [19] Yang, X. *et al.* Terahertz-light quantum tuning of a metastable emergent phase hidden by superconductivity. *Nat. Mater.* **17**, 586 (2018).
- [20] Cea, T., Castellani, C. & Benfatto, L. Nonlinear optical effects and third-harmonic generation in superconductors: Cooper pairs versus Higgs mode contribution. *Phys. Rev. B* **93**, 180507 (2016).
- [21] Murotani, Y. & Shimano, R. Nonlinear optical response of collective modes in multiband superconductors assisted by nonmagnetic impurities. *Phys. Rev. B* **99**, 224510 (2019).
- [22] Krull, H., Bittner, N., Uhrig, G., Manske, D. & Schnyder, A. Coupling of Higgs and Leggett modes in non-equilibrium superconductors. *Nat. Commun.* **7**, 11921 (2016).
- [23] Vaswani, C. *et al.* Light quantum control of persisting Higgs modes in iron-based superconductors. *Nat. Commun.* **12**, 258 (2021).
- [24] Giorgianni, F. *et al.* Leggett mode controlled by light pulses. *Nat. Phys.* **15**, 341–346 (2019).
- [25] Udina, M., Cea, T. & Benfatto, L. Theory of coherent-oscillations generation in terahertz pump-probe spectroscopy: From phonons to electronic collective modes. *Phys. Rev. B* **100**, 165131 (2019).
- [26] Chu, H. *et al.* Phase-resolved Higgs response in superconducting cuprates. *Nature Commun.* **11**, 1793 (2020).

- [27] Schwarz, L., Fauseweh, B. & Tsuji, N. e. a. Classification and characterization of nonequilibrium Higgs modes in unconventional superconductors. *Nat. Commun.* **11**, 287 (2020).
- [28] Moor, A., Volkov, A. F. & Efetov, K. B. Amplitude Higgs mode and admittance in superconductors with a moving condensate. *Phys. Rev. Lett.* **118**, 047001 (2017).
- [29] Puviani, M., Schwarz, L., Zhang, X.-X., Kaiser, S. & Manske, D. Current-assisted Raman activation of the Higgs mode in superconductors. *Phys. Rev. B* **101**, 220507 (2020).
- [30] Cundiff, S. T. & Mukamel, S. Optical multidimensional coherent spectroscopy. *Physics Today* **66**, 44–49 (2013).
- [31] Kuehn, W., Reimann, K., Woerner, M., Elsaesser, T. & Hey, R. Two-dimensional terahertz correlation spectra of electronic excitations in semiconductor quantum wells. *J. Phys. Chem. B* **115**, 5448–5455 (2011).
- [32] Junginger, F. *et al.* Nonperturbative interband response of a bulk InSb semiconductor driven off resonantly by terahertz electromagnetic few-cycle pulses. *Phys. Rev. Lett.* **109**, 147403 (2012).
- [33] Lu, J. *et al.* Coherent two-dimensional terahertz magnetic resonance spectroscopy of collective spin waves. *Phys. Rev. Lett.* **118**, 207204 (2017).
- [34] Johnson, C. L., Knighton, B. E. & Johnson, J. A. Distinguishing nonlinear terahertz excitation pathways with two-dimensional spectroscopy. *Phys. Rev. Lett.* **122**, 073901 (2019).
- [35] Mootz, M., Luo, L., Wang, J. & Perakis, I. E. Visualization and quantum control of light-accelerated condensates by terahertz multi-dimensional coherent spectroscopy. *Communications Physics* **5**, 47 (2022).

- [36] Mahmood, F., Chaudhuri, D., Gopalakrishnan, S., Nandkishore, R. & Armitage, N. P. Observation of a marginal Fermi glass. *Nature Physics* **17**, 627–631 (2021).
- [37] Mootz, M., Wang, J. & Perakis, I. E. Lightwave terahertz quantum manipulation of nonequilibrium superconductor phases and their collective modes. *Phys. Rev. B* **102**, 054517 (2020).
- [38] Lee, S. *et al.* Template engineering of Co-doped BaFe<sub>2</sub>As<sub>2</sub> single-crystal thin films. *Nat. Mater.* **9**, 397–402 (2010).
- [39] Tu, J. J. *et al.* Optical properties of the iron arsenic superconductor BaFe<sub>1.85</sub>Cco<sub>0.15</sub>As<sub>2</sub>. *Phys. Rev. B* **82**, 174509 (2010).
- [40] Charnukha, A. Optical conductivity of iron-based superconductors. *J. Phys.: Condens. Matter.* **26**, 253203 (2014).
- [41] Stephen, M. J. Transport equations for superconductors. *Phys. Rev.* **139**, A197–A205 (1965).
- [42] Yang, F. & Wu, M. W. Gauge-invariant microscopic kinetic theory of superconductivity: Application to the optical response of Nambu-Goldstone and Higgs modes. *Phys. Rev. B* **100**, 104513 (2019).
- [43] Anderson, P. W. Random-phase approximation in the theory of superconductivity. *Phys. Rev.* **112**, 1900–1916 (1958).
- [44] Nambu, Y. Quasi-particles and gauge invariance in the theory of superconductivity. *Phys. Rev.* **117**, 648–663 (1960).
- [45] Liu, C. *et al.* Evidence for a Lifshitz transition in electron-doped iron arsenic superconductors at the onset of superconductivity. *Nature Physics* **6**, 419–423 (2010).

- [46] Fernandes, R. M. & Schmalian, J. Competing order and nature of the pairing state in the iron pnictides. *Phys. Rev. B* **82**, 014521 (2010).
- [47] Yang, X. *et al.* Nonequilibrium pair breaking in  $\text{Ba}(\text{Fe}_{1-x}\text{Co}_x)_2\text{As}_2$  superconductors: Evidence for formation of a photoinduced excitonic state. *Phys. Rev. Lett.* **121**, 267001 (2018).

## Acknowledgments

THz spectroscopy work was supported by National Science Foundation 1905981 (M.M.). THz MDCS instrument was supported by the W.M. Keck Foundation (initial design and commission) and by the U.S. Department of Energy, Office of Science, National Quantum Information Science Research Centers, Superconducting Quantum Materials and Systems Center (SQMS) under the contract No. DE-AC02-07CH11359 (upgrade for improved cryogenic operation). THz spectral analysis was supported by the Ames Laboratory, the US Department of Energy, Office of Science, Basic Energy Sciences, Materials Science and Engineering Division under contract No. DEAC0207CH11358 (L.L.). The work at UW-Madison (synthesis and characterizations of epitaxial thin films) was supported by the US Department of Energy (DOE), Office of Science, Office of Basic Energy Sciences (BES), under award number DE-FG02-06ER46327. Modeling work at the University of Alabama, Birmingham was supported by the US Department of Energy under contract # DE-SC0019137 and was made possible in part by a grant for high performance computing resources and technical support from the Alabama Supercomputer Authority.